Effect of pH waves on capacitive charging in microfluidic flow channels

Ionics (2014) 20:1315–1322
DOI 10.1007/s11581-014-1083-6

ORIGINAL PAPER

Effect of pH waves on capacitive charging in microfluidic flow channels

Susan H. Roelofs · Michiel van Soestbergen · Mathieu Odijk · Jan C. T. Eijkel · Albert van den Berg

Received: 30 September 2013 / Revised: 29 January 2014 / Accepted: 30 January 2014 / Published online: 7 March 2014

Abstract Novel energy-efficient desalination techniques, such as capacitive deionization (CDI), are a key element for the future of the fresh water supply, which is increasingly under stress due to the ever-growing world population and ongoing climate changes. CDI is a desalination technique where salt ions are removed from a flow channel by the application of an electrical potential difference across this channel and are stored in electrical double layers. The aim of this work is to visualize and explain the charging process of CDI using a new microfluidic approach. Namely, we implement the geometry of CDI on a chip and visualize the ion distributions in the channel using fluorescence microscopy. In contrast to normal CDI, our system was operated in the absence of flow, using non-porous electrodes. By using two pH-sensitive fluorescence dyes, we found the formation of pH waves across the channel, even though the system is operated at low potential differences in order to suppress Faradaic reactions, such as water splitting. From simulations of the transport process, we found that a small current density in the order of 0.1 A m^{-2} can trigger the formation of such pH waves. CDI generally benefits from large electrode areas relative to the channel cross section. However, this large area ratio will also increase the magnitude of these waves, which might lead to a reduction in desalination efficiency.

Keywords Capacitive deionization · Desalination · pH · Fluorescence · Lab-on-chip

S. H. Roelofs (✉) · M. Odijk · J. C. T. Eijkel · A. van den Berg
MESA+ Institute for Nanotechnology, University of Twente,
PO Box 217, 7500 AE Enschede, The Netherlands
e-mail: s.h.roelofs@utwente.nl

M. Odijk
e-mail: m.odijk@utwente.nl

J. C. T. Eijkel
e-mail: j.c.t.eijkel@utwente.nl

A. van den Berg
e-mail: a.vandenberg@utwente.nl

M. van Soestbergen
Department of Applied Physics, Eindhoven University of Technology, PO Box 513, 5600, MB Eindhoven, The Netherlands
e-mail: michiel.van.soestbergen@tue.nl

Introduction

The availability of fresh water is one of the major challenges of the twenty-first century, and the necessity of an energy-efficient desalination technology is more urgent than ever [1–3]. Namely, the demand for fresh water is increasing due to population growth and rapid economic development [1], while fresh water aquifers suffer from salt water intrusion along coastal lines, [1] and climate change leads to less reliable rainfall and drier soils [2]. If the current trend in increasing water scarcity continues, 75 % of the world population will face fresh water shortage by 2050 [3], even affecting the more industrialized nations in North America and Europe [1]. Desalination of salt and/or brackish water can provide a solution to reduce this fresh water scarcity [1].

Distillation and reverse osmosis are the most common desalination methods for large-scale fresh water production. However, these methods require either high temperatures or high pressures over ion exchange membranes and are thus not energy efficient. An alternative approach is to electrokinetically desalinate water using capacitive deionization (CDI) [4]. A typical CDI device consists of salt water flowing through a microfluidic flow channel having two electrodes at opposite sides of this channel. Upon the application of an electrical potential difference between these electrodes, ions migrate to the oppositely biased electrode and are stored in the electrical double layer at the surface of the electrode, where they screen the applied potential [5]. During charging, desalinated water leaves the system until the electrodes become saturated. The system is regenerated by removing the

charge. During this release step, a concentrated electrolyte (brine) exits the system. This cycle is repeated to produce desalinated water in a batch-wise manner. The main advantages of CDI are as follows: the technology is potentially energy efficient for desalination of brackish water (electrical energy can even be recycled during the release step) [6–8], whereas it requires less expensive parts, such as pumps operating at high pressure [9]. The coupling of CDI and recycling of energy through capacitive mixing or "capmix" were recently suggested [10, 11]. Consequently, CDI is an energy-efficient desalination method at low capital costs.

Up till now, research on CDI has been performed mainly on macroscale systems, with typical capacities in the order of liters per minute [5, 12]. The main focus of interest included (i) regeneration speed and efficiency of the electrode material for ion storage capacity and (ii) increase of energy efficiency and ion selectivity [13–18]. The approach in these studies has been to measure the ion concentrations of the in and effluent water stream in order to determine the response of the entire system [5, 9, 13, 19–22]. In this work, we will use a chip-scale device, which allows for local (fluorescent) imaging of the ion concentration profiles in the flow channel to locally study ion transport. In contrast to a traditional CDI system, our chip is operated under no-flow conditions, with non-porous electrodes. A microfluidic CDI device was recently used by Demirer and Hidrovo to demonstrate the potential of fluorescence imaging of the salt profile in the flow channel [23]. Our focus in this study, however, is on the formation of acidic and alkaline regions, i.e., pH waves, throughout this channel. It has been shown previously that these pH waves can severely hinder the electrokinetic remediation of e.g., soils [24] or porous building materials [25]. The origin of pH variations arising in electrolytes is often related to Faradaic electrode reactions [26–28], whereas capacitive-induced pH variations due to locally released protons from a silicon nitride wall have been observed as well [29]. Consequently, the formation of acidic and alkaline regions is a surface effect that is largely enhanced in the flow channel of CDI systems due to their large electrode surface area relative to the volume of the flow channel [30]. The pioneering work by Soffer et al. demonstrated already in 1972 acidic regions upon the application of a positive potential at the electrodes in a CDI system [30]; however, this was measured in the effluent stream of the system. Therefore, in this work, we will study the formation of pH waves in the microfluidic flow channels of CDI devices.

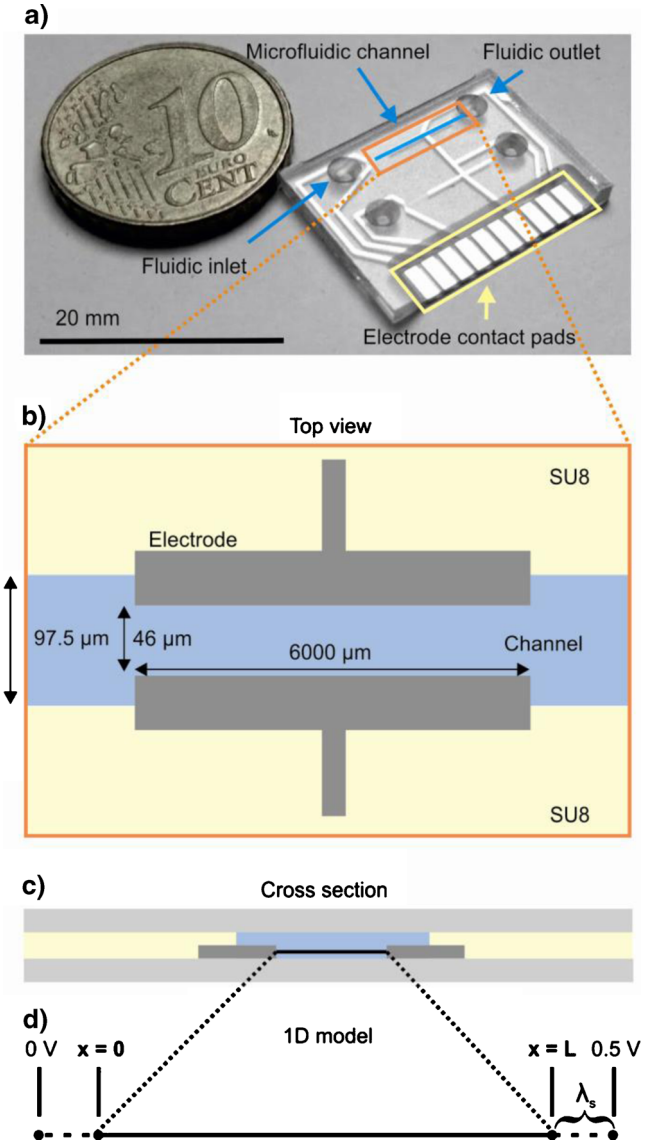

Fig. 1 (**a**) Picture of the microfluidic chip. The electrode contact pads are marked *yellow*. The microfluidic channel is situated in between the fluidic in- and outlet and is marked in *blue*. (**b**, **c**) Schematic of the microfluidic channel. The CDI electrodes are situated within the same plane and partly in the channel, such that the liquid can flow over the electrodes. (**b**) Top view of the microchannel. (**c**) Cross section of the channel. (**d**) Schematic overview of the 1D simulation geometry. The boundaries, at $x=0$ and $x=L$, correspond to the Stern layers of both electrodes, with λ_S as the Stern layer thickness

Materials and methods

Experimental

The microfluidic device that is used for the experiments is depicted in Fig. 1. In this figure, we also give schematics of the top view of the 97.5-µm-wide microfluidic channel. The electrodes are relatively long (6 mm) to make sure that edge effects, such as a non-homogenous electric field, can be neglected. The cross-sectional view shows that the chip consists of a top wafer (Borofloat glass) containing powder-blasted in- and outlet holes, which is bonded to a bottom wafer (Borofloat glass) using a patterned epoxy layer (SU-8). The height of the channel is ~7 µm, which is large compared to the electrode height of 120 nm. The electrodes are

fabricated from platinum and are positioned co-planar on the bottom wafer.

The charging behavior of our CDI system was visualized by fluorescence microscopy. Two solutions containing a 0.1-mM fluorescent dye dissolved in ultrapure water were used. One contained BODIPY (BOD), with an excitation wavelength (λ_{ex}) of 492 nm and an emission wavelength (λ_{em}) of 515 nm (Invitrogen), and the other contained fluorescein (FL), λ_{ex}=490 nm and λ_{em}=514 nm (Sigma-Aldrich). FL is known for its pH-dependent emission [31], whereas BOD is relatively stable [32]. At the excitation wavelength of 490 nm, the divalent anion is the main contributor to the fluorescence intensity for both dyes [33]. Both FL and BOD have Na^+ as the counterion. The solutions were sequentially inserted into the microfluidic channel, through gas impermeable syringes and tubing. The intensity gradient of the fluorescent dyes in the channel was monitored over time with a CCD camera (Hamamatsu, c4742-80-12AG) connected to an inverted microscope (Leica, DMI5000M) with a filter cube (Leica, L5) having an excitation bandpass of 480 ±20 nm and an emission bandpass of 527±15 nm. Excitation took place from below with a mercury lamp. The diffraction-limited spot size, determined by the objective, is 600–800 nm.

A potential pulse with a magnitude of 0.5 V, a frequency of 0.1 Hz, and a pulse width of 1 s (dutycycle of 10 %) was applied across the two electrodes using a waveform generator (Agilent, 33220A/20 MHz). At this applied potential, it is expected that, with an estimated capacitance of platinum of 20 μF cm-2, 5-10% of the fluorescent dye can be removed from the reservoir. The electrical current was obtained by measuring the voltage drop across a calibrated resistor placed in series with the chip by using an oscilloscope (Tektronix, TCS 2002C).

Theory

In this section, we present a simulation model for the microfluidic CDI device using the 1D geometry depicted in Fig. 1d. We will use this model to distinguish between the effects of charge transport and pH variations on the measured fluorescence intensity profiles. Using this geometry, it is expected that the simulated concentration profiles will be qualitatively similar to the experimental observations but will differ in magnitude. One of the key factors causing these deviations is the fact that the absorption of ions on top of the electrodes is not accounted for. The model is based on the classical Poisson-Nernst-Planck theory, which describes the transport of ions and electrical potential distribution in the microfluidic CDI system. Here, the flux of ions (J_i) is given by the Nernst-Planck equation, which combined with a mass balance becomes

$$\frac{dC_i}{dt} = -\frac{\partial J_i}{\partial x} + \sum r_j = \frac{\partial}{\partial x} D_i \left(\frac{\partial C_i}{\partial x} + C_i \frac{z_i F}{RT} \frac{\partial V}{\partial x} \right) + \sum r_j, \quad (1)$$

where C_i is the ion concentration [mol m^{-3}] of species i, t is the time [s], r_j is the chemical reaction rate [mol s^{-1} m^{-3}], D_i is the diffusion coefficient [m^2 s^{-1}], z_i is the valence [−], V is the electrical potential [V], F is the Faraday constant [C mol^{-1}], R is the gas constant [J K^{-1} mol^{-1}], T is the temperature [K], and x is the distance [m] as indicated in Fig. 1d. The experiments were performed under no-flow conditions; therefore, advection was not included in our calculations. The electrical potential is calculated using the Poisson equation, $\varepsilon \partial^2 V/\partial x^2 = -\rho$, which relates the charge density, $\rho = \sum z_i C$ [C m^{-3}], to the electric potential, where ε is the electrical permittivity [F m^{-1}].

We assume that BOD can deprotonate in an alkaline environment according to

$$BOD^{2-} \rightleftharpoons BOD^{3-} + H^+, \quad pKa = 8, \quad (2)$$

where pKa is the acidic dissociation constant, which relates the concentration of protonated, C_{prot}, and deprotonated, C_{dep}, species according to $pKa = -\log(C_{dep}C_H/C_{prot})$. FL is very susceptible to protonate and is in this respect often used as a pH indicator dye [34–36]. The corresponding chemical reactions for FL are as follows:

$$FL^0 \rightleftharpoons FL^- + H^+, \quad pKa = 4.34, \quad (3a)$$

$$FL^- \rightleftharpoons FL^{2-} + H^+, \quad pKa = 6.78. \quad (3b)$$

Furthermore, we consider the self-dissociation of water,

$$H_2O \rightleftharpoons OH^- + H^+, \quad (4)$$

for which we have the equilibrium condition, $C_H C_{OH} = K_w$, where K_w is the equilibrium constant of this reaction and equals 10^{+8} mol^2 m^{-6} under normal conditions. The reaction rates for Eqs. (2), (3)a, and (3)b at constant temperature are described by $r_j = k_r(10^{-pKa} C_{prot} - C_{dep} C_H)$, where k_r is the reverse rate constant. To simplify the systems of equations, we eliminate the reaction rate constants for the self-dissociation of water by assuming that Eq. (4) remains at equilibrium. We do this by defining the model parameter $\rho_w = C_H - C_{OH}$, for which the self-dissociation reaction rate cancels [37, 38]. From the equilibrium condition for water dissociation and the expression for ρ_w, the following expressions for C_H and C_{OH} can be determined:

$C_H = \frac{1}{2}\left(\sqrt{4K_w + \rho_w^2} + \rho_w\right)$ and $C_{OH} = \frac{1}{2}\left(\sqrt{4K_W + \rho_W^2} - \rho_W\right)$. The mass balance of Eq. (1) for

ρ_w after substitution of the expressions for C_H and C_{OH} thus becomes [25]

$$\frac{\mathrm{d}\rho_w}{\mathrm{d}t} = \frac{1}{2}\frac{\partial}{\partial x}\sum_i \left\{ D_i \left(\frac{z_i \rho_w}{\sqrt{4k_w + {\rho_w}^2}} + 1 \right) \frac{\partial \rho_w}{\partial x} + \frac{F}{RT}\left(\sqrt{4k_w + {\rho_w}^2} + z_i \rho_w \right) \frac{\partial V}{\partial x} \right\} + \sum r_j, \quad (5)$$

where index i indicates either H or OH and index j runs over the remaining rates of FL and BOD.

The boundaries of our system are at the plane of closest approach of the ions. The area between the plane of closest approach and the electrode remains charge free, is known as the Stern layer, and has a thickness of λ_S. The potential drop across this layer, ΔV_S, must be either added to, or subtracted from, the electrode potential, V_{app}, according to $V = V_{app} \pm \lambda_s \partial V/\partial x$, where ± sign refers to the positive value at $x=0$ and the negative value at $x=L$. Additionally, we have no-flux boundary conditions, $J_i=0$, for all species at all boundaries except for ρ_w at the platinum electrodes, where we have the generalized Frumkin-Butler-Volmer equation [39, 40],

$$J_{\rho_w} = K_\rho \left\{ C_{\mathrm{OH}} \exp\left(\frac{1}{2}\frac{F}{RT}\Delta V_S \right) - C^0_{\mathrm{OH}} \exp\left(-\frac{1}{2}\frac{F}{RT}\Delta V_S \right) \right\}, \quad (6a)$$

at $x=0$ and

$$J_{\rho_w} = K_\rho \left\{ C_{\mathrm{H}} \exp\left(-\frac{1}{2}\frac{F}{RT}\Delta V_S \right) - C^0_{\mathrm{H}} \exp\left(\frac{1}{2}\frac{F}{RT}\Delta V_S \right) \right\}, \quad (6b)$$

at $x=L$, where K_ρ is a rate constant and superscript 0 indicates the concentration at $t=0$. Consequently, Eq. (6) relates the electrical current due to water splitting to the local potential drop across the Stern layer, ΔV_S.

Results and discussion

Results of the fluorescence measurements

Figure 2a shows a snapshot of a typical example of a fluorescence intensity measurement. In the supplementary material, videos are given of the measurements for both BOD and FL. In Fig. 2b and c, a cross section of the fluorescence intensity profiles in the presence of either BOD or FL over a period of 1,000 ms is shown. Upon the application of 0.5 V, the double layer is charged, and a variation in fluorescence intensity is observed across the channel. The measured intensity is proportional to the concentration of BOD and FL in their divalent state. For BOD, a rapid initial change in the intensity is observed, which leads to a linear intensity profile that remains stationary until ~500 ms. After this initial increase, the profiles start to flatten again until at 1,000 ms, the initial profile ($t=0$) is retained. For FL, also a rapid initial change in intensity is observed. However, this change is initially only in the vicinity of the electrodes; after which, the intensity spreads out to form a linear profile. Contrary to BOD, this linear profile remains its shape up to 1,000 ms.

Both dyes show a counterintuitive behavior. First, we expect that the overall concentration of the dyes decreases due to

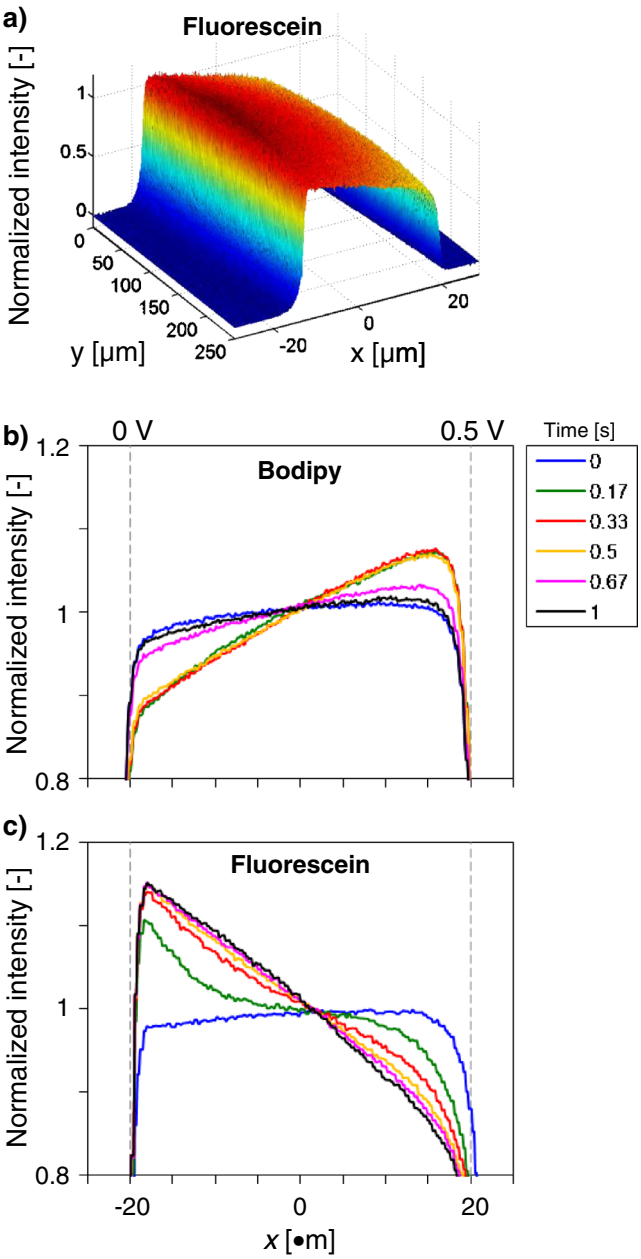

Fig. 2 Fluorescence intensity measurements: (**a**) example of a snapshot of the measured fluorescein profile across the flow channel and (**b**) cross section of the intensity profile of BOD and (**c**) FL over a period of 1 s, respectively

accumulation of ions in the double layers. This effect is in both cases negligible. Second, if ions were depleted from the channel, we would expect a simultaneous decrease of the concentration of the dye at both electrodes due to electroneutrality across the flow channel [41]. However, a simultaneous decrease at both sides of the profiles is not observed. Finally, the intensity profiles show a linear shape with opposite slopes: a positive slope for BOD and a negative slope for FL. These three anomalies indicate that the observed effect is not only a capacitive behavior but also comprises pH variations as we will demonstrate in the next section using the simulations.

Simulation results

For the simulations, the input parameters as discussed below are used. For the sake of simplicity, we assume equal diffusion coefficients for all ionic states of the BOD and FL dyes. Consequently, a diffusion coefficient of $4.25 \cdot 10^{-10}$ m^2 s^{-1} (see ref. 42) and $1.13 \cdot 10^{-9}$ (see ref. 43) m^2 s^{-1} is assumed for the FL and BOD ions, respectively. The values for the remaining diffusion coefficients are $1.33 \cdot 10^{-9}$ m^2 s^{-1} for Na^+, $9.3 \cdot 10^{-9}$ m^2 s^{-1} for H^+, and $5.27 \cdot 10^{-9}$ m^2 s^{-1} for OH^- [44]. The electrical permittivity is $78 \cdot 8.854 \cdot 10^{-12}$ F/m. For both dyes, an initial pH equal to 7 is assumed. The protonation reactions of the FL dye are fast [45]. As a result, we will use K=1,000 m^3 mol^{-1} s^{-1} for these reactions, since higher values of this number did not affect the outcome of the simulations. The thickness of the Stern layer was set to $\lambda_S = 3 \cdot 10^{-9}$ m. This number is higher than might be expected from the value of the hydrated radius of most common ions [46]. However, the ions of the fluorescent dyes used in this work are relatively large, whereas the Stern layer thickness might also include the effect of a decreased electrical permittivity due to dipole alignment at high electrode potentials [47]. We have adjusted the length of the cell in order to account for the extra volume in the in- and outlet of the channel. Namely, this extra volume will affect the amount of desalination since ions can diffuse from this "dead volume" into the channel between the electrodes. To account for this effect, we use L=80 μm for the length of the cell, which in combination with the above-mentioned value for the Stern layer thickness results in a negligible desalination level as found in the experiments on Fig. 2. The rate constant of the electrochemical reaction, K_ρ, is set to 2 m s^{-1}.

The simulated pH profiles as well as the ion distributions of the fluorescent dye in case of BOD are plotted in Fig. 3 for several time steps. First, we consider the case where the chemical conversion from the divalent BOD ion into its trivalent state is absent. This situation is equivalent to the pH variation that would be observed in the system in the presence of an inorganic salt like Na_2SO_4. Here, we see that a pH wave develops as indicated by the dashed line in Fig. 3a. This wave has an acidic region near the anode (0.5 V) at x=L and an alkaline region near the cathode (0 V) at x=0 due to the local

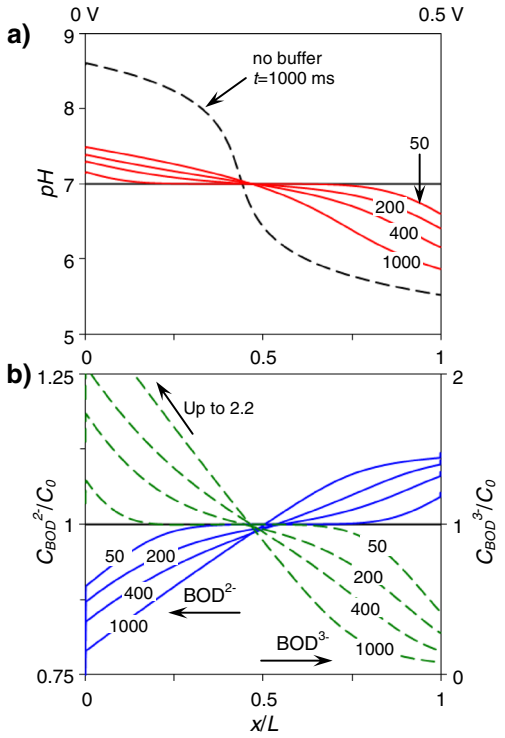

Fig. 3 Simulation results for BOD: (**a**) pH profiles for different time steps (*solid lines*) and the solution in the absence of the protonation reaction (*dashed line*) which corresponds to the pH change occurring in the presence of an inorganic salt like Na_2SO_4 and (**b**) distribution of BOD^{2-} (*blue lines*) and BOD^{3-} (*green lines*) for different time steps. The time steps are indicated in milliseconds in the labels

oxidation and reduction reaction, which proceeds at these electrodes, respectively. By considering the conversion of divalent BOD into trivalent ions, we add some pH buffer capacity to the system. This can be observed by the solid lines in Fig. 3b. Here, we see that the pH wave is suppressed by the above-mentioned chemical conversion. This suppression is more dominant in the alkaline region due to the pKa value of this reaction, which is set to 8. In this region, the divalent BOD ions are converted into trivalent ions as shown in Fig. 3a, whereas in the acidic region, the divalent BOD ions prevail. This results in a BOD^{2-} profile with an increasing concentration from x=0 to x=L, which is similar to the observed profile in Fig. 2b. The deviation from a linear profile in the acidic region might be due to our one-dimensional approach. For BOD^{2-} to increase linear in the region from x/L equals to ~0.75 up to 1, the concentration of BOD^{3-} needs to increase as well, which is not possible in our simulations due to mass conservation. In the experiments, BOD^{3-} might be supplied from elsewhere in the system, e.g., the dead volume in the in- and outlet channel, so that the concentration in this region will increase. The fading of the measured fluorescent profiles for BOD at prolonged time might be the result of poisoning of the electrodes, e.g., due to the deposition of oxidized BOD.

The simulated profiles for the FL dye are given in Fig. 4. Again, we find the formation of a pH wave in the absence of any chemical conversions, as shown by the dashed line in Fig. 4a. Similar to BOD, the FL dye will act as a pH buffer when these chemical conversions are considered. However, FL is a better buffer in the acidic region due to its lower p*K*a values compared to BOD. This can be seen by the solid lines in Fig. 4a, where the pH wave is more suppressed in the acidic region than in the alkaline region. The conversion processes for FL are also opposite to that observed for BOD. Namely, in the alkaline region, the concentration of FL^{2-} increases, whereas FL^{-} and FL^{0} are depleted in this region, as observed in Fig. 4b–d. In the acidic region, the concentration of FL^{2-} decreases and the concentration of FL^{-} and FL^{0} increases. As a result, the concentration of FL^{2-}, which is proportional with the measured fluorescent intensity, shows a decreasing profile from $x=0$ to $x=L$, as observed in Fig. 2c. This explains the opposite slopes for the intensity profiles in Fig. 2b and c. Namely, BOD will lose its fluorescent intensity in an alkaline environment due to the loss of a proton, see Eq. (2), whereas the intensity of FL will increase in a more alkaline environment due to the deprotonation of FL^{0} and FL^{-}, see Eq. (3).

The calculated electrical current through the system is presented in Fig. 5. This electrical current, I, is composed of two parts given by $I = -\varepsilon \frac{\mathrm{d}}{\mathrm{d}t}\frac{\partial \varphi}{\partial x} \pm FJ$, where the first term represents the Maxwell displacement current, and the second term originates from the Faradaic processes (i.e., electrochemical charge transfer) at the electrodes [40]. The displacement current describes the charge accumulation in the double layers, which contributes dominantly to the transient part of the curves, whereas the Faradaic processes dominate the steady-state part. The steady-state current is predicted to be ~2 nA (0.05 mA m^{-2}) for both the system containing BOD as well as for the system containing FL. From our experience, the detection limit is ~5 nA. Note that the predicted 2 nA is below the detection limit of our experimental equipment, which explains the systematic error between the measured and calculated data in Fig. 5. Water splitting also occurs at a potential of 0.5 V, which is well below the water-splitting potential, and is observed as a leakage current. Consequently, the potential might still be sufficiently large to explain the counterintuitive experimental results as presented in Fig. 2.

Though the magnitude of the pH waves given in Figs. 3 and 4 does not appear very large, they might be enhanced in practical CDI systems. Namely, CDI systems generally use porous electrodes with relative surface areas of 1,000 m^2/g [18], whereas in our system, the electrode area is only ~5 times the cross-sectional area of the microfluidic flow channel. A Faradaic leakage current scales to some extent with the surface area in the presence of a convective flow and might thus result in a pH wave with a larger magnitude than observed in this work, which can hinder the desalination

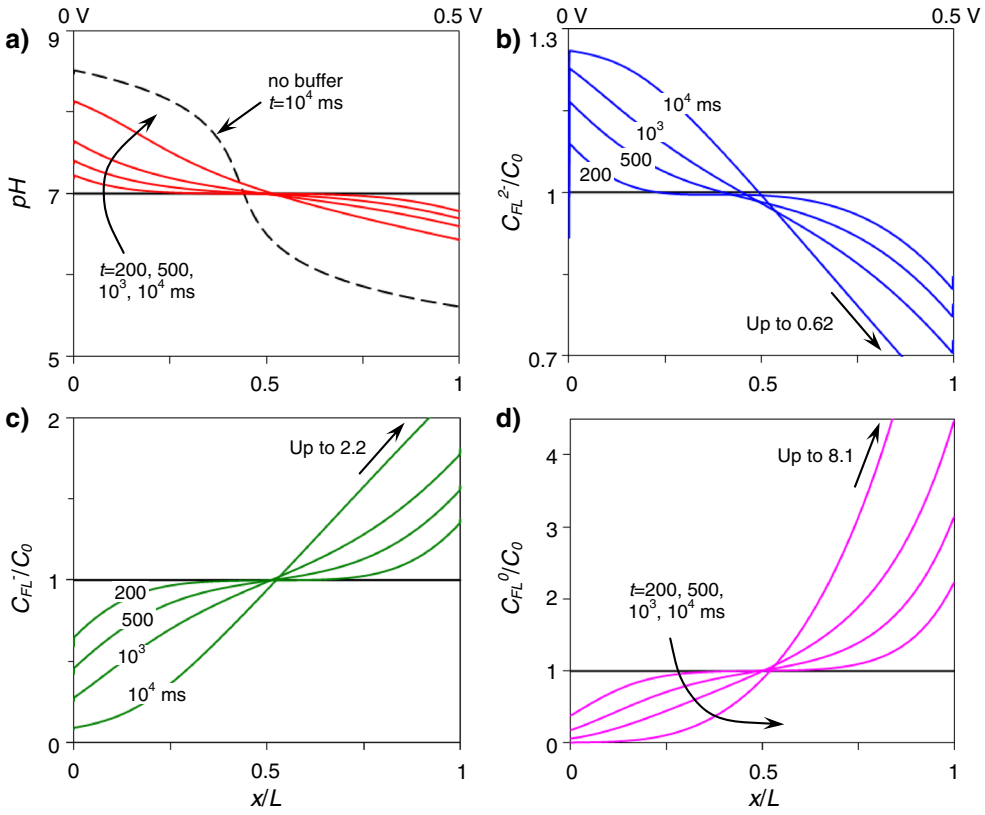

Fig. 4 Simulation results for FL: (**a**) pH profiles for different time steps and (**b**) distribution of FL^{2-} (*blue lines*), (**c**) FL^{-} (*green lines*), and (**d**) FL^{0} (*purple lines*) for different time steps. The values for the time steps are in milliseconds

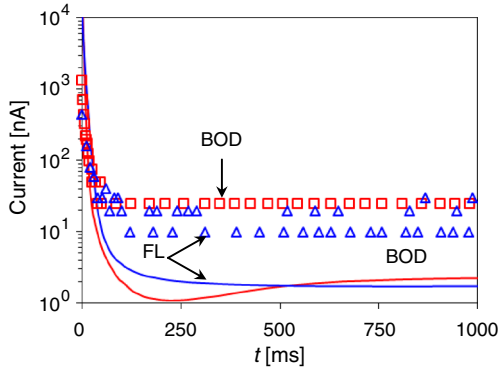

Fig. 5 Electrical current flowing through the system as a function of time. The symbols indicate the measured data, and the full lines the computed results

performance of a CDI device. First, acidic or alkaline environments can trigger chemical reactions that impede the desalination performance. For example, many kinds of metal ions will form insoluble hydroxide complexes in a highly alkaline environment, pH>10 [24, 48], which might precipitate and clog the microfluidic channel. Secondly, as the microfluidic channel gets desalinated, the pH wave will form a sharp front at which locally a large gradient in electrical potential develops, which reduces the electrical field strength in the remainder of the channel. The reduced electrical field strength will reduce the migration of ions and thus the desalination rate. On the other hand, pH buffers such as phosphate or ammonium might be present in the water stream as well. pH buffers have a stabilizing effect on the pH in solutions [49] and might therefore reduce the magnitude of the pH wave.

Conclusions

We have demonstrated experimentally as well as computationally the formation of pH waves in a microfluidic CDI device. The charging process of the CDI system was visualized through fluorescence microscopy, in the absence of background electrolytes and pH buffers. The most pronounced observed effect is the opposite gradient in intensity across the channel for the dyes BODIPY and fluorescein. This counterintuitive behavior suggests the formation of pH waves even though the system was operated within the non-Faradaic regime with an applied potential of 0.5 V. Our computational results show that pH variations are causing this counterintuitive behavior. A leakage current on the order of 2 nA indicates dissociation of water resulting in a flux of H^+ and OH^- ions at the electrodes which locally changes the pH. The fluorescent dyes in the channel function as pH buffers with a valence-dependent fluorescence intensity, resulting in the observed intensity profiles. The understanding of pH variations in a CDI device can be important for optimizing the desalination rate of CDI systems.

Acknowledgement The authors gratefully acknowledge P. M. Biesheuvel (Wageningen University, The Netherlands) for fruitful discussions.

References

1. Shannon MA, Bohn PW, Elimelech M, Georgiadis JG, Mariñas BJ, Mayes AM (2008) Science and technology for water purification in the coming decades. Nature 452:301
2. Marris E (2008)Water: More crop per drop. Nature 452:273
3. Hightower M, Pierce SA (2008) The energy challenge. Nature 452: 285
4. Porada S, Zhao R, van der Wal A, Presser V, Biesheuvel PM (2013) Review on the science and technology of water desalination by capacitive deionization. Prog Mater Sci 58:1388
5. Welgemoed TJ, Schutte CF (2005) Capacitive Deionization Technology: An alternative desalination solution. Desalination 183: 327
6. Długołęcki P, van der Wal Environ A (2013) Energy Recovery in Membrane Capacitive Deionization. Sci Technol 47:4904
7. Brogioli D (2009) Document Extracting renewable energy from a salinity difference using a capacitor. Phys Rev Lett 103:058501
8. Brogioli D, Zhao R, Biesheuvel PM (2011) A prototype cell for extracting energy from a water salinity difference by means of double layer expansion in nanoporous carbon electrodes. Energy Environ Sci 4:772
9. Farmer JC, Fix DV, Mack GV, Pekala RW, Poco JF (1996) Capacitive deionization of NaCI and $NaNO_3$ solutions with carbon aerogel electrodes. J Electrochem Soc 143:159
10. Rica RA, Ziano R, Salerno D, Mantegazza F, van Roij R, Brogioli D (2013) Capacitive Mixing for Harvesting the Free Energy of Solutions at Different Concentrations. Entropy 15:1388
11. Rica RA, Ziano R, Salerno D, Mantegazza F, Brogioli D (2012) Thermodynamic Relation between voltage-concentration dependence and salt adsorption in electrochemical cells. Phys Rev Lett 109:156103
12. Mossad M, Zhang W, Zou L (2013) Using capacitive deionisation for inland brackish groundwater desalination in a remote location. Desalination 308:154
13. Zhao R, van Soestbergen M, Rijnaarts HHM, van der Wal A, Bazant MZ, Biesheuvel PM (2012) Time-dependent ion selectivity in capacitive charging of porous electrodes. J Coll Int Sci 384:38
14. Biesheuvel PM, Zhao R, Porada S, van der Wal A (2011) Theory of membrane capacitive deionization including the effect of the electrode pore space. J Coll Int Sci 360:239
15. Zou L, Li L, Song H, Morris G (2008) Using mesoporous carbon electrodes for brackishwater desalination. Water Res 42:2340
16. Li H, Zou L, Pan L, Sun Z (2010) Novel Graphene-Like Electrodes for Capacitive Deionization. Env Sci Technol 44:8692
17. Porada S, Bryjak M, van der Wal A, Biesheuvel PM (2012) Effect of electrode thickness variation on operation of capacitive deionization. Electrochim Acta 75:148
18. Zhao R, Satpradit O, Rijnaarts HHM, Biesheuvel PM, van der Wal A (2013) Optimization of salt adsorption rate in membrane capacitive deionization. Water Res 47:1941
19. Oren Y, Soffer A (1983) Water desalting by means of electrochemical parametric pumping. I. The equilibrium properties of a batch unit cell. Journal of Applied Electrochemistry 13:473
20. Johnson AM, Newman J (1971) Desalting by Means of Porous Carbon Electrodes. J Electrochem Soc 118:510
21. Biesheuvel PM, Bazant MZ (2010) Nonlinear dynamics of capacitive charging and desalination by porous electrodes. Phys Rev E 81: 031502

22. Anderson MA, Cudero AL, Palma J (2010) Capacitive deionization as an electrochemical means of saving energy and delivering clean water. Comparison to present desalination practices: Will it compete? Electrochim Acta 55:3845
23. Demirer ON, Hidrovo CH (2013) Laser-induced fluorescence visualization of ion transport in a pseudo-porous capacitive deionization microstructure. Microfluids and Nanofluids (in press)
24. Probstein RF, Hicks RE (1993) Removal of contaminants from soils by electric fields. Science 260:498
25. Kamran K, van Soestbergen M, Huinink HP, Pel L (2012) Inhibition of electrokinetic ion transport in porous materials due to potential drops induced by electrolysis. Electrochim Acta 78:229
26. Lee J-H, Bae W-S, Choi J-H (2010) Electrode reactions and adsorption/desorption performance related to the applied potential in a capacitive deionization process. Desalination 258:159
27. Lee J-B, Park K-K, Eum H-M, Lee C-W (2006) Desalination of a thermal power plant wastewater by membrane capacitive deionization. Desalination 196:125
28. Bouhadana Y, Avraham E, Noked M, Ben-Tzion M, Soffer A, Aurbach D (2011) Capacitive Deionization of NaCl Solutions at Non-Steady-State Conditions: Inversion Functionality of the Carbon Electrodes. J Phys Chem C 115:16567
29. Veenhuis RBH, van der Wouden EJ, van Nieuwkasteele JW, van den Berg A, Eijkel JCT (2009) Field-effect based attomole titrations in nanoconfinement. Lab Chip 9:3472
30. Soffer A, Folman M (1972) The electrical double layer of high surface porous carbon electrode. J Electroanal Chem Int Electrochem 38:25
31. Diehl H, Markuszewski R (1989) Studies on fluorescein-VII. The fluorescence of fluorescein as a function of pH. Talanta 36:416
32. Shao J, Guo H, Ji S, Zhao J (2011) Styryl-BODIPY based red-emitting fluorescent OFF–ON molecular probe for specific detection of cysteine. Biosens Bioelectron 26:3012
33. Klonis N, Sawyer WH (1996) Spectral Properties of the Prototropic Forms of Fluorescein in Aqueous Solution. J Fluoresc 6:147
34. Fiedler S, Hagedom R, Schnelle T, Richter E, Wagner B, Fuhr G (1995) Diffusional Electrotitration: Generation of pH Gradients over Arrays of Ultramicroelectrodes Detected by Fluorescence. Anal Chem 67:820
35. Alodan MA, Smyrl WH (1998) Detection of localized corrosion of aluminum alloys using fluorescence microscopy. J Electrochem Soc 145:1571
36. Suss ME, Mani A, Zangle TA, Santiago JG (2011) Electroosmotic pump performance is affected by concentration polarizations of both electrodes and pump. Sensors Actuators A 165:310
37. van Soestbergen M, Mavinkurve A, Rongen RTH, Jansen KMB, Ernst LJ, Zhang GQ (2010) Theory of aluminum metallization corrosion in microelectronics. Electrochim Acta 55:5459
38. Andersen MB, van Soestbergen M, Mani A, Bruus H, Biesheuvel PM, Bazant MZ (2012) Current-induced membrane discharge. Phys Rev Lett 109:108301
39. Biesheuvel PM, van Soestbergen M, Bazant MZ (2009) Imposed currents in galvanic cells. Electrochim Acta 54:4857
40. van Soestbergen M, Biesheuvel PM, Bazant MZ (2010) Diffuse-charge effects on the transient response of electrochemical cells. Phys Rev E 81:021503
41. Kamran K, van Soestbergen M, Pel L (2013) Electrokinetic Salt Removal from Porous Building Materials Using Ion Exchange Membranes. Trans Porous Media 96:221
42. Culbertson CT, Jacobson SC, Ramsey JM (2002) Diffusion coefficient measurements in microfluidic devices. Talanta 56:365
43. Mavré F, Anand RK, Laws DR, Chow K-F, Chang B-Y, Crooks JA, Crooks RM (2010) Bipolar electrodes: A useful tool for concentration, separation, and detection of analytes in microelectrochemical systems. Anal Chem 82:8766
44. Newman JS (1973) Electrochemical systems. Prentice-Hall, Englewood Cliffs
45. Alvarez-Pez JM, Ballesteros L, Talavera E, Yguerabide J (2001) Fluorescein excited-state proton exchange reactions: Nanosecond emission kinetics and correlation with steady-state fluorescence intensity. J Phys Chem A 105:6320
46. Nightingale ER (1959) Phenomenological theory of ion solvation - effective radii of hydrated ions. J Phys Chem 63:1381
47. Kilic MS, Bazant MZ, Ajdari A (2007) Steric effects in the dynamics of electrolytes at large applied voltages. I. Double-layer charging. Phys Rev E 75:021502
48. Avraham E, Bouhadana Y, Soffer A, Aurbach D (2009) Limitation of Charge efficiency in capacitive deionization: I. on the behavior of single activated carbon. J Electrochem Soc 156:95
49. Persat A, Chambers RD, Santiago JG (2009) Basic principles of electrolyte chemistry for microfluidic electrokinetics. Part I: Acid-base equilibria and pH buffers. Lab Chip 9:2437